Mon. Not. R. Astron. Soc. **000**, 000–000 (0000) Printed 19 February 2016 (MN LATEX style file v2.2)

Two bi-stability jumps in theoretical wind models for massive stars and the implications for Luminous Blue Variable supernovae

Blagovest Petrov⋆, Jorick S. Vink and Götz Gräfener
Armagh Observatory, College Hill, Armagh, BT61 9DG, Northern Ireland

arXiv:1602.05868v1 [astro-ph.SR] 18 Feb 2016

Accepted 2016 February 16. Received 2016 February 16; in original form 2015 April 1

ABSTRACT

Luminous Blue Variables have been suggested to be the direct progenitors of supernova types IIb and IIn, with enhanced mass loss prior to explosion. However, the mechanism of this mass loss is not yet known. Here, we investigate the qualitative behaviour of theoretical stellar wind mass-loss as a function of $T_{\rm eff}$ across two bi-stability jumps in blue supergiant regime and also in proximity to the Eddington limit, relevant for LBVs. To investigate the physical ingredients that play a role in the radiative acceleration we calculate blue supergiant wind models with the CMFGEN non-LTE model atmosphere code over an effective temperature range between 30 000 and 8 800 K. Although our aim is not to provide new mass-loss rates for BA supergiants, we study and confirm the existence of two bi-stability jumps in mass-loss rates predicted by Vink, de Koter, & Lamers (1999). However, they are found to occur at somewhat lower $T_{\rm eff}$ (20 000 and 9 000 K, respectively) than found previously, which would imply that stars may evolve towards lower $T_{\rm eff}$ before strong mass-loss is induced by the bi-stability jumps. When the combined effects of the second bi-stability jump and the proximity to Eddington limit are accounted for, we find a dramatic increase in the mass-loss rate by up to a factor of 30. Further investigation of both bi-stability jumps is expected to lead to a better understanding of discrepancies between empirical modelling and theoretical mass-loss rates reported in the literature, and to provide key inputs for the evolution of both normal AB supergiants and LBVs, as well as their subsequent supernova type II explosions.

Key words: stars: mass loss – stars: supergiants – stars: atmospheres – stars: winds, outflows

1 INTRODUCTION

Luminous Blue Variables (LBVs) are unstable massive stars in close proximity to the Eddington limit (Humphreys & Davidson 1994; Vink 2012). They are characterised by strong stellar winds (with mass-loss rates of up to 10^{-3} $M_\odot\,yr^{-1}$) and large variations in their visual magnitudes ($\Delta V \simeq 1-2$) due to variable radii and $T_{\rm eff}$ in the range $\sim 8\,000 - 30\,000$ K. During these "S Doradus" excursions LBVs cross the temperature range of two bi-stability jumps (BSJ), which is expected to lead to winds with variable mass-loss rate and terminal velocity (Vink, de Koter, & Lamers 1999; Vink & de Koter 2002; Groh, Hillier, & Damineli 2011).

Traditionally, stellar evolution models have considered LBVs to be in a transitory phase between H-burning O-type stars and He-burning Wolf-Rayet stars (Langer et al. 1994; Maeder & Meynet 2000; Ekström et al. 2012). However, this has not been supported by recent observations which indicate that some LBVs might be direct progenitors of both supernovae (SNe) type IIb and IIn (Kotak & Vink 2006; Smith et al. 2007; Trundle et al. 2008; Gal-Yam & Leonard 2009). More recently, evolutionary calculations of both single stars (Groh, Meynet, & Ekström 2013) and binary mergers (Justham et al. 2014) have been able to reproduce LBVs as direct SN type II progenitors.

If LBVs are indeed in a direct pre-SN state, the fact that they reside in close proximity to the Eddington and bi-stability limits, may dramatically affect their mass-loss rates prior to explosion. Indeed, both SN IIn (Kiewe et al. 2012; Ofek et al. 2013; Moriya et al. 2014) and IIb SNe, such as 2013cu (Gal-Yam et al. 2014; Groh 2014; Gräfener & Vink 2016) seem to have been subjected to increased mass loss prior to explosion. This increased mass loss is oftentimes attributed to "eruptive" mass loss (Smith 2015), although a physical mechanism for such eruptive mass loss has not been agreed upon. The wave-driven mass-loss mechanism by Shiode & Quataert (2014) may be a good candidate, but how this would produce an outflow has yet to be determined. The most promising scenario for eruptive mass loss has been proposed by Owocki et al. (2004), who developed a theory of 'porosity-moderated mass loss' (see also Shaviv 1998, 2000). As LBVs find themselves in close proximity to the Eddington limit, we can be confident that radiation pressure will play a role in the driving of an outflow (Owocki 2015;

⋆ E-mail: bvp@arm.ac.uk

Vink 2015). This is even more likely now that empirical mass-loss rates in close proximity to the Eddington limit have been found to increase steeply (Bestenlehner et al. 2014) – in agreement with theoretical expectations of Gräfener et al. (2011); Vink et al. (2011); Vink & Gräfener (2012).

Eruptive mass loss has also been proposed as a necessary ingredient in the overall mass loss of massive stars during their lives. The reason that the stellar wind mass-loss rates during the O-star phase have been reduced, as empirical O star mass-loss rates have been down-revised due to wind clumping. However, as these reduced rates agree reasonably well (within a factor of 2 to 3) with the theoretical rates of Vink, de Koter, & Lamers (2000, 2001) that are commonly used in stellar evolution models (Martins & Palacios 2013), it is not so clear eruptive mass loss is relevant (see also Khan et al. 2015) . Instead, stellar winds in the OBA supergiant range likely dominate over those of early O star mass-loss rates (Groh et al. 2014).

The bi-stability jump (Pauldrach & Puls 1990) is observed as a drop in the ratio between the terminal and escape velocities ($v_\infty/v_{\rm esc}$) of B-type supergiants (Bsgs) by a factor 2, when the effective temperature ($T_{\rm eff}$) falls below ~21 000 K (Lamers et al. 1995; Crowther et al. 2006; Markova & Puls 2008; Garcia et al. 2014). Vink et al. (1999) showed that this was the result of the recombination of the dominant wind driver from Fe IV to Fe III. They also predicted that this drop should be accompanied by a jump in the mass-loss rate ($\dot{M}$) which may have been confirmed *qualitatively* by Benaglia et al. (2007), but significant inconsistencies between theoretical and empirical mass-loss rates have also remained (Vink et al. 2000; Trundle et al. 2004; Trundle & Lennon 2005; Crowther, Lennon, & Walborn 2006). These discrepancies might be due to the issues of wind clumping (Massa et al. 2003; Bouret, Lanz, & Hillier 2005; Puls et al. 2006; Fullerton, Massa, & Prinja 2006; Davies, Vink, & Oudmaijer 2007; Puls, Vink, & Najarro 2008), inadequate treatment of macro-clumping and porosity effects (Oskinova et al. 2007; Prinja & Massa 2010; Sundqvist et al. 2010, 2011; Muijres et al. 2011; Šurlan et al. 2012; Petrov et al. 2014). In any case, the existence of the predicted bi-stability jump regarding $\dot{M}$ is not yet conclusive and an independent investigation of it is needed.

Recent massive star evolution models, such as the Geneva models of Groh et al. (2014), show that most of the mass loss occurs due to stellar winds in the later supergiant phase, rather than during the early O-star phase near the zero-age main sequence (ZAMS).

The reason that O star mass-loss rates have been reduced is that empirical O star mass-loss rates have been down-revised by a factor of 2-3 due to wind clumping (Repolust et al. 2004; Mokiem et al. 2007; Shenar et al. 2015). Currently, there is an ongoing debate whether the theoretical O star mass-loss rates are correct. The outcome will strongly depend on future progress in modelling optically thin and thick clumping in radiative transfer and alternative wind-modelling, as performed in the present paper. The temperature dependence of the mass-loss rate is also of key importance when analysing the accuracy and suitability of mass-loss recipes for the effects of mass loss through stellar winds in massive star evolution.

Whilst the existence of the $\dot{M}$ jump is still under debate, other data are unambiguous: the wind velocities of O stars and early Bsgs are considerably larger those of the later Bsgs. This is likely to imply significant differences in mass-loss rates of Bsgs in both temperature domains. It is matter of adequate interpretation of the observations and/or treatment of the models to establish whether the trends are gradual (Crowther et al. 2006) or steep (Lamers et al. 1995; Vink et al. 1999).

Lamers et al. (1995) and Vink et al. (1999) suggested that there might be also be a second bi-stability jump near 10 000 K which has not been studied in detail yet. In this paper, we investigate whether the second bi-stability jump exists, in conjunction with studying the behaviour of the first bi-stability jump near ~21 000 K. Whilst the second jump could provide new insights into the properties of late B and A supergiants, for LBVs both bi-stability jumps are relevant, as their $T_{\rm eff}$ changes over a range between ~ 8000 and 30 000 K (*e.g.* van Genderen 2001; Vink 2012). Therefore, if we understand the temperature behaviour of $\dot{M}$, we might be able to explain some of the mass loss variations during the different LBV phases (Vink & de Koter 2002). However, the effects of luminosity, clumping and metallicity on $\dot{M}$ needs to be properly understood.

The contents of the paper is as follows. In § 2 we briefly describe the method that we use to predict $\dot{M}$ as well as our grid of models. The main results of current investigation are outlined and discussed in § 3, whilst in § 4 we compare mass loss rates following from the CMFGEN models to the mass-loss rates resulting from the Monte Carlo calculations of Vink et al. (2000, 2001) (V00/V01). In § 5, we discuss the importance of the bi-stability jumps in $\dot{M}$ for the behaviour of LBVs. Finally, in § 6 conclusions are drawn.

2 WIND MODELLING

Our current investigation utilises sophisticated fully line-blanketed atmosphere models computed with the non-LTE radiative transfer code CMFGEN (Hillier & Miller 1998). CMFGEN is designed to solve the statistical equilibrium and radiative transfer equations in spherical geometry. Thus, the code is able to calculate the mass absorption coefficient k_ν, and the total line acceleration, $g_{\rm L}^{\rm tot}$, which can be integrated directly:

$$g_{\rm L}^{\rm tot} = \frac{1}{c}\int_0^\infty F_\nu k_\nu^{\rm L}{\rm d}\nu, \tag{1}$$

where the stellar flux F_ν and $k_\nu^{\rm L}$ are computed on a relevant frequency grid.

When $g_{\rm L}^{\rm tot}$ is known one may predict mass-loss rates of massive stars, as their winds are driven by the radiative pressure in spectral lines.

2.1 $Q_{\rm wind}$ – a tool to determine $\dot{M}$

In order to predict $\dot{M}$, we compare the radiative energy lost due to all line-interactions, which is used to lift the mass out of the potential well and to accelerate the wind to v_∞, $W_{\rm wind}$:

$$W_{\rm wind} = \dot{M}\int_{R_\star}^\infty \left(g_{\rm rad} - \frac{1}{\rho}\frac{{\rm d}p}{{\rm d}r}\right){\rm d}r, \tag{2}$$

to the total energy of the wind, $L_{\rm wind}$ (see for details Abbott & Lucy 1985; Vink et al. 1999):

$$L_{\rm wind} = \dot{M}\left(\frac{1}{2}v_\infty^2 + \frac{G{\rm M}_\star}{R_\star}\right). \tag{3}$$

This is similar to the work ratio method, $Q_{\rm wind} = W_{\rm wind}/L_{\rm wind}$, used by Gräfener, Koesterke, & Hamann (2002); Gräfener & Hamann (2005) to check the consistency of their models. Note that in Eq. 2, $g_{\rm rad}$ does not only refer to line-interactions, but it includes all processes which contribute to the radiative acceleration (*e.g.* Thomson scattering, bound-free acceleration).

If the radiative acceleration provides sufficient force to lift a certain amount of mass, $\dot{M}$, out of the potential well, then $Q_{\rm wind}$

Table 1. Prescribed stellar and wind parameters for the grid of models.

$\log L/L_\odot$	$M_\star$ ($M_\odot$)	Γ_e	$Z/Z_\odot$	$T_{\rm eff}$ (K)	$\dot{M}$ ($10^{-6}\,M_\odot\,yr^{-1}$)	model series
5.50	40, 30, 20	0.19, 0.26, 0.39	0.1, 0.2, 0.5, 0.75, 1	8800 – 30000	0.1 – 2	L5.5
5.75	71	0.19	0.2, 0.5, 1	8800 – 30000	0.1 – 2	L5.75M71

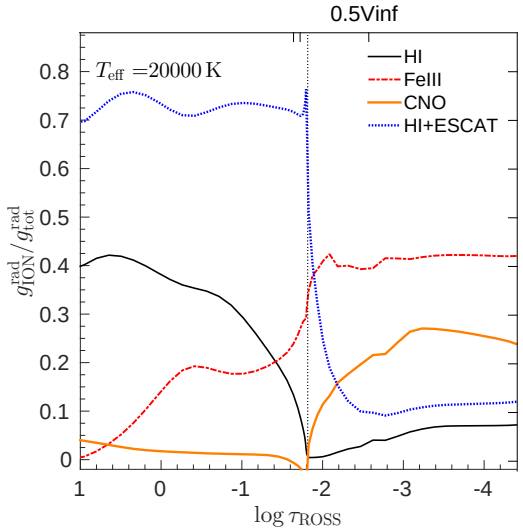

Figure 1. Relative contribution of individual ions to the total radiative force for model from model series 'L5.5M40' with $\dot{M} = 0.5\times10^{-6}\,M_\odot\,yr^{-1}$. The largest part of the H I acceleration is due to bound-free processes

.

is expected to be of order unity. If $Q_{\rm wind} << 1$, then the radiative acceleration cannot support a wind with mass-loss rate, $\dot{M}$.

It should be stated that CMFGEN does not currently solve the wind momentum equation. Therefore, the wind velocity structure has to be prescribed. In our models, the wind velocity structure is described by a standard β-type velocity law with $\beta = 1$, which is joined to the hydrostatic part of the wind just below the sonic point. The prescribed velocity structure might differ from the one obtained from the radiative acceleration. However, for different velocity laws one might obtain better agreement between the adopted and acquired velocity structures. Therefore, $Q_{\rm wind}$ still provides a meaningful criterion to establish whether the stellar wind can be driven, and used as an approximate tool to determine $\dot{M}$ from models with specific stellar parameters.

2.2 The grid of models

We have calculated a grid of wind models covering a range of $T_{\rm eff}$ and $\log g$ appropriate for blue supergiants, which include the ions of C, N, O, Ne, Mg, Al, Si, P, S, Ar, Ca, and Fe (with model atoms summarised in Table A1). Observations indicate that stellar winds are inhomogeneous, and therefore modelling non-homogeneous stellar atmospheres becomes necessary.

Currently CMFGEN is only able to take optically thin (micro) clumping into account. This micro-clumping approach is based on the hypothesis that the wind consists of small-scale over-density "clumps" which are optically thin. The density ρ within these clumps is assumed to be enhanced by a clumping factor D compared to the mean wind density $\bar{\rho}$. This factor can also be understood in terms of volume filling factor $f = D^{-1}$, assuming that the inter-clump medium is void. Most of our models are non-homogeneous and are calculated with $f_\infty = 0.1$, described by the following exponential law:

$$f(r) = f_\infty + (1 - f_\infty)\exp(-v(r)/v_{\rm cl}), \quad (4)$$

where $v_{\rm cl}$ is the velocity at which clumping is switched on. We have chosen the clumping to start at $v_{\rm cl} = 30$ km s^{-1}, i.e. just above the sonic point. In § 3.2 however, we calculated a set of homogeneous models in order to estimate the influence of micro clumping on the bi-stability jump.

To investigate whether the dependence of $\dot{M}$ on $T_{\rm eff}$ is universal, we calculated model series with different luminosities and masses in such a way that the *classical* Eddington parameter, Γ_e, is unchanged. Unless otherwise stated, our CMFGEN models have been computed for 1/2 solar metal abundances[1], in order to be relevant for results of the VLT-FLAMES Tarantula Survey (Evans et al. 2011; Bestenlehner et al. 2014; McEvoy et al. 2015). We adopt the parameters summarised in Table 1. For the main set of models we select masses $M_\star = 40, 30$, and $20\,M_\odot$ in order to compare our results to the $\dot{M}$ calculations of Vink et al. (2001) and to have the rough possibility to have Bsgs as core hydrogen burning main-sequence stars as well as core helium burning stars (see *e.g.* Vink et al. 2010). For the models with $\log L_\star/L_\odot = 5.75$ we select $M_\star = 71\,M_\odot$ in order to achieve the same mass to luminosity ratio as the models with $\log L_\star/L_\odot = 5.50$ and $M_\star = 40\,M_\odot$.

The wind terminal velocities, v_∞, were adopted according to the observed relations between v_∞ and $v_{\rm esc}$, *i.e.* $v_\infty/v_{\rm esc} = 2.6$ for $T_{\rm eff} \gtrsim 21000$ K, $v_\infty/v_{\rm esc} = 0.7$ for $T_{\rm eff} \lesssim 10000$ K and $v_\infty/v_{\rm esc} = 1.3$ for $T_{\rm eff}$ in between (Lamers et al. 1995; Crowther et al. 2006; Markova & Puls 2008; Garcia et al. 2014). Here, the escape velocity is given by:

$$v_{\rm esc} = \sqrt{\frac{2GM_\star}{R_\star}}, \quad (5)$$

where $M_\star$ is mass of the star, and $R_\star$ is its radius.

The definition of $v_{\rm esc}$ here is not corrected for the radiation pressure by electron scattering and therefore is different from the one used by Vink et al. (1999). Consequently, the applied terminal velocities in present work are somewhat overestimated, when the values of 2.6, 1.3 and 0.7 are used, and the predicted $\dot{M}$ might be underestimated. Overall, however, the influence should be small, except for those models with large Γ_e.

In the present investigation we did not intend to make quantitative predictions. Our models do not reach a similar level of completeness as those calculated by Vink et al. (1999). Whilst we might

[1] The reference solar abundances of Asplund et al. (2009) were adopted.

be missing the high-lying Fe lines and other elements from the Periodic Table in the current investigation, Vink et al. (1999) preselected the important driving lines out of a total line list of millions bound-bound transitions from Kurucz (1988) from the first 30 elements in the Periodic Table (H - Zn). In other words, with the Monte Carlo method Vink et al. (1999) were fairly complete and until we have similar level of completeness, we will refrain from making quantitative radiative acceleration predictions. Instead, the aim of current paper is to investigate *qualitatively* both bi-stability jumps in $\dot{M}$ that were predicted by Vink et al. (1999).

3 RESULTS

3.1 Identity of the main line drivers

By calculating Eq. 1 with the opacities of different ions, we were able to extract the contribution of individual ions to the total acceleration. As an example, in Fig. 1, we show the relative contribution of individual ions to the total radiative force for a model from the 'L5.5' series with mass, $M_\star = 40\,M_\odot$ ('L5.5M40'). The model has $T_{\rm eff} = 20\,000$ K, $\dot{M} = 0.5\times10^{-6} M_\odot\,{\rm yr}^{-1}$.

Close to the star, most of the radiative force is provided by neutral hydrogen (H I) and electron scattering (blue dashed line)[2], whilst the most important line driver in the outer wind is Fe III. The presented contributions to the total radiative force are distance dependent and it is thus ambiguous to establish which of the ions provide most of the global wind acceleration. Therefore, in Fig. 2, we investigate which ions contribute mostly to the work ratio, $Q_{\rm wind}$.

In our CMFGEN models, the location of the lower boundary where $Q_{\rm wind}$ is calculated is defined at $\tau_{\rm ROSS} = 100$. However, if the lower boundary is set at wind velocities $\sim 0.2\times v_\infty$, $W_{\rm wind}$ changes by only a few percent, *i.e.* $W_{\rm wind}$ is mainly determined in the supersonic part of the wind. Also, the pressure contribution to $W_{\rm wind}$ (and thus to $Q_{\rm wind}$) is only relevant in the sub-sonic wind-region. Consequently, the pressure term does not play an important role in the calculation of the total $W_{\rm wind}$ ($Q_{\rm wind}$).

The left hand-side of Fig. 2 depicts the behaviour of $Q_{\rm wind}$ as a function of $T_{\rm eff}$ in model series 'L5.5M40' with fixed $\dot{M}$. $Q_{\rm wind}$ is decreasing when $T_{\rm eff}$ is reduced between 30 000 and 25 000 K and also between 20 000 and 10 000 K, whilst between 22 500 and 20 000 K a discontinuity in $Q_{\rm wind}$ is produced. The reasons for this are two-fold: (i) a change in Fe ionisation balance; and (ii) the different velocity ratio, $v_\infty/v_{\rm esc}$, for the models on both sides of the B-supergiant domain. For low values of $v_\infty/v_{\rm esc}$ ($T_{\rm eff} \leqslant 20\,000$ K), $Q_{\rm wind} = 1$ should be easier to achieve in comparison to models with higher values of $v_\infty/v_{\rm esc}$ ($T_{\rm eff} \geqslant 22\,500$ K).

3.1.1 Acceleration by CNO

The right-hand side of Fig. 2 displays the relative contribution of individual ions to $Q_{\rm wind}$. For simplicity, only the contributions of important ions are presented. On the hot side of the bi-stability jump (at $T_{\rm eff} \gtrsim 22\,500$) the ions of C,N, and O contribute mostly to $Q_{\rm wind}$. Thus, they contribute mostly to the line acceleration and they are important line drivers in hotter models. However, when $T_{\rm eff}$ is reduced from 25 000 to 20 000 K, the contribution of CNO to $Q_{\rm wind}$ decreases in a favour of Fe group elements (chiefly Fe III). A similar finding was reported by Abbott (1982), but he did not make a distinction between the inner and outer wind. Vink et al. (1999) used the so-called sonic point, the point at which the wind reaches the local speed of sound, to distinguish the inner from the outer wind. Vink et al. (1999) used this point as a physical point beyond which the mass-loss rate is already fixed but the wind terminal velocity has yet to be determined (see also Puls et al. 2000).

3.1.2 Iron - the wind driver

Figure 3 displays that when $T_{\rm eff}$ is reduced from 25 000 to 22 500 K, Fe IV decreases in favour of Fe III. Even though Fe IV is still the dominant ionisation stage in the cooler model, most of the radiative force of iron comes from Fe III (*cf. right-hand side* of Fig. 2). When $T_{\rm eff}$ is further reduced to 20 000 K, Fe III becomes the dominant ionisation stage and now provides about 40% of $Q_{\rm wind}$.

The reader should be aware that we have prescribed $v_\infty/v_{\rm esc} = 1.3$ for models with $T_{\rm eff}$ between 20 000 and 10 000 K in line with the observations (see *e.g.* Markova & Puls 2008). Thus, the models on the cool edge of the bi-stability jump would achieve more "easily" the prescribed wind velocities than those models at the hot side, where the velocities are higher. In addition, lower velocities would also lead to higher densities (continuity equation), which stimulate recombinations. Consequently, between 22 500 and 20 000 K, a jump in $Q_{\rm wind}$ is produced. Note that this jump has to be accompanied by a jump in $\dot{M}$ as well, because the model with $T_{\rm eff} = 20\,000$ K would be able to drive a stronger wind. This is in agreement with previous studies (Vink et al. 1999, 2001), although CMFGEN predicts a jump at $T_{\rm eff} \simeq 20\,000$ K, whilst according to the Monte-Carlo calculations the jump is expected at somewhat hotter temperatures, at $T_{\rm eff} \simeq 25\,000$ K.

Monte-Carlo calculations now have an improved line driving treatment (see *e.g.* Müller & Vink 2008; Muijres et al. 2012) and therefore a discordance in temperature of 5 000 K between CMFGEN and Monte-Carlo models is particularly intriguing. Such a large discordance may underline fundamental differences between the assumptions regarding the treatment of the ionisation in both codes, or the discordance might be caused by differences in the atomic data which both codes use. The main difference between the CMFGEN models and the Monte-Carlo calculations is probably the 'exact' vs simplified Non-LTE treatment, which was calculated by V00/V01 using the ISA-Wind code (de Koter et al. 1993). This is the most likely reason for the discrepancies, as the ISA-Wind calculations do not include line blanketing and therefore the iron ionisation would occur at higher $T_{\rm eff}$ in comparison to CMFGEN models.

3.2 Bi-stability jump on trial

CMFGEN does not currently calculate mass-loss rates. Instead, $\dot{M}$ is required as an input parameter. Nevertheless, as was discussed earlier, the $Q_{\rm wind}$ ratio enables us in some way to estimate for which value of $\dot{M}$, a specific model is able to drive its stellar wind. For models with given set of stellar parameters we predict their mass-loss rate by adopting several values of $\dot{M}$. The value of $\dot{M}$ for which $Q_{\rm wind}$ becomes unity is the predicted mass-loss rate.

To find out for which $\dot{M}$ our models acquire $Q_{\rm wind} \approx 1$, we investigate the behaviour of $Q_{\rm wind}$ as a function of $\dot{M}$ and $T_{\rm eff}$. On the *left hand-side* of Fig. 4, we present a contour plot of $Q_{\rm wind}$ depending on $T_{\rm eff}$ and $\dot{M}$ in model series 'L5.5M40' with $v_\infty/v_{\rm esc} = 2$, $f_\infty = 0.1$, and $v_{\rm cl} = 30$ km/s. The figure demonstrates that for a constant velocity ratio, between 22 500 and 20 000 K, the predicted $\dot{M}$ is increased by a factor of about two. The temperature location of

[2] Radiative acceleration of H I (black solid) is mainly determined by bound-free processes

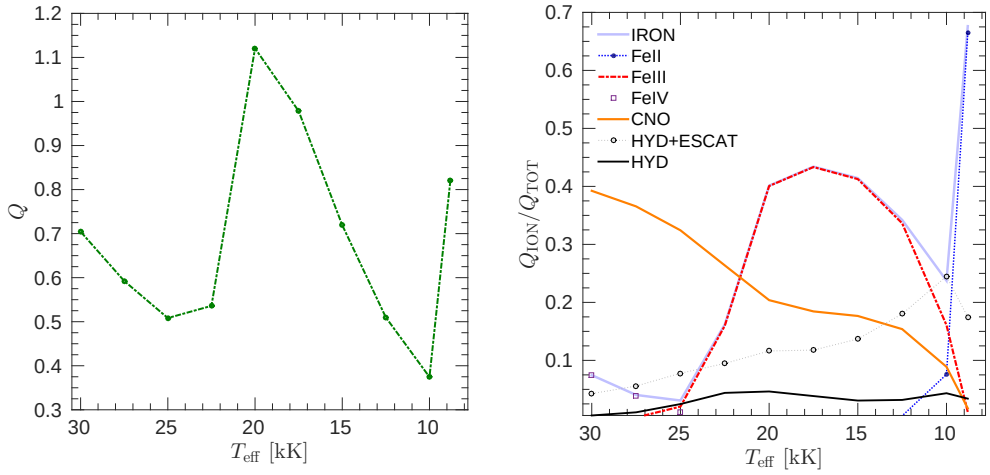

Figure 2. *Left*: $Q_{\rm wind}$ vs $T_{\rm eff}$ for models from 'L5.5M40' series with fixed mass-loss rate of $\dot{M} = 0.5\times10^{-6}\,{\rm M}_\odot\,{\rm yr}^{-1}$. Observed velocity ratios of $v_\infty/v_{\rm esc} = 2.6$ for $T_{\rm eff} \geqslant 22\,500$ K, $v_\infty/v_{\rm esc} = 1.3$ for $T_{\rm eff} \in [10\,000\,{\rm K}, 20\,000\,{\rm K}]$, and $v_\infty/v_{\rm esc} = 0.7$ for $T_{\rm eff} < 10\,000$ K are applied. *Right*: relative contribution of individual ions to the corresponding work ratio, $Q_{\rm wind}$.

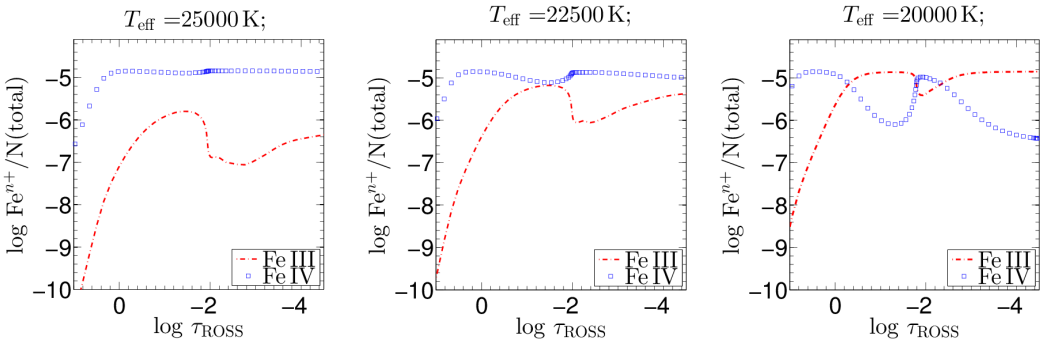

Figure 3. Change in ionisation balance between Feıv and Feıii in models from 'L5.5M40' series with $\dot{M} = 0.5\times10^{-6}\,{\rm M}_\odot\,{\rm yr}^{-1}$.

the predicted increase in $\dot{M}$ is in good correspondence to observational findings (see *e.g.* Markova & Puls 2008). If the observed velocity ratios are applied (*i.e.* $v_\infty/v_{\rm esc} = 2.6$ for $T_{\rm eff} \geqslant 22\,500$ K and $v_\infty/v_{\rm esc} = 1.3$ for $T_{\rm eff}$ between 20 000 and 10 000 K), then $\dot{M}$ is increased by about a factor of four (*cf. right-hand side* of Fig. 4). On the basis of Fig. 2 we confirm that Feıii is indeed responsible for this jump.

In Fig. 5, we show contour plots of the relative contribution of the ions of C, N, and O (*left*), and iron (*right*) to the total $Q_{\rm wind}$ ratio. It is interesting to note that with an increase of $\dot{M}$ the contribution of C, N, and O to $Q_{\rm wind}$ is decreased in favour of iron. When $\dot{M}$ is increased by about three times in the models with $T_{\rm eff} \sim 20\,000 - 17\,500$ K, the contribution of iron (chiefly Feıii) to $Q_{\rm wind}$ is increased by about 25% ($Q_{\rm Fe}/Q_{\rm wind}$ increases from 0.4 to 0.5). This is because in stronger winds the recombinations of Feıv to Feıii are favoured and the absolute number of iron ions increases.

The red dashed iso-contours on the *left-hand side of* Fig. 4 display the behaviour of $Q_{\rm wind}$ as a function of $T_{\rm eff}$ and $\dot{M}$ in homogeneous sets of models with fixed velocity ratio of $v_\infty/v_{\rm esc} = 2$. Note that micro-clumping has a large impact on $Q_{\rm wind}$ for temperatures between $\sim 17\,500$ and $\sim 22\,500$ K, *i.e.* around the bi-stability jump location. For the other temperatures the influence of micro-clumping is less important. Moreover, the temperature at which bi-stability jump occurs in the homogeneous set of models ($T_{\rm eff} = 17\,500$ K) is lower in comparison to the initial set of models with $f_\infty = 0.1$, $v_{\rm cl} = 30$ km/s. Thus, the degree of clumping seems to be an important parameter for the temperature location of the bi-stability-jump. We found that in model series with values for $v_{\rm cl}$ up to 200 km/s, the bi-stability jump occurs at $T_{\rm eff} = 20\,000$ K and therefore $v_{\rm cl}$ has little effect on the temperature location of the bi-stability jump.

3.3 A second bi-stability jump?

To investigate whether a second jump in $\dot{M}$ exist near $T_{\rm eff} = 10\,000$ K, we have calculated additional models with $T_{\rm eff} = 8\,800$ K[3]. For $T_{\rm eff} \lesssim 10\,000$ K Lamers et al. (1995) found that $v_\infty/v_{\rm esc} = 0.7$ and therefore, we used such velocity ratio for those models. The reader should be aware that the terminal velocities of stars with temperatures below 10 000 K were measured with an accuracy between 10% and 20% and therefore the value of $v_\infty/v_{\rm esc} = 0.7$ might be uncertain.

Nevertheless, we consider the adopted value as reasonable because: (i) in our coolest models the ions of Feıı provide most of the line acceleration (*cf. right hand-side of* Fig. 2), which is in agreement with previous investigations (*e.g.* Vink et al. 1999; Vink & de Koter 2002), and therefore Feıı could influence v_∞ and $\dot{M}$; and (ii) the temperature range where Feıı becomes the main line-driver

[3] Below 8 800 K, a self-consistent hydrostatic solution in the hydrostatic part of wind was not obtained and therefore our grid stops at 8 800 K.

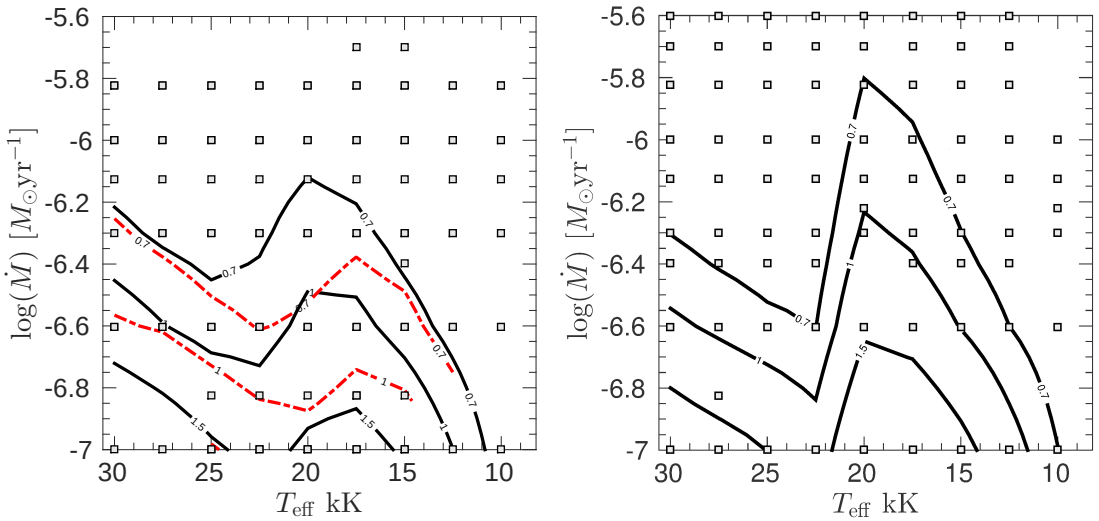

Figure 4. *Left*: contour plot of $Q_{\rm wind}$ as a function of $T_{\rm eff}$ and $\dot{M}$ in model series 'L5.5M40' with $v_\infty/v_{\rm esc} = 2$. To see the effect of clumping, iso-contours from models with no micro-clumping taken into account are over-plotted with red dashed lines. *Right*: contour plot of $Q_{\rm wind}$ from the same model series but with observed ratio of $v_\infty/v_{\rm esc} = 2.6$ for $T_{\rm eff} >\sim 21\,000\,K$ and $v_\infty/v_{\rm esc} = 1.3$ for $T_{\rm eff} <\sim 21\,000\,K$. White squares mark the positions of the of the calculated models.

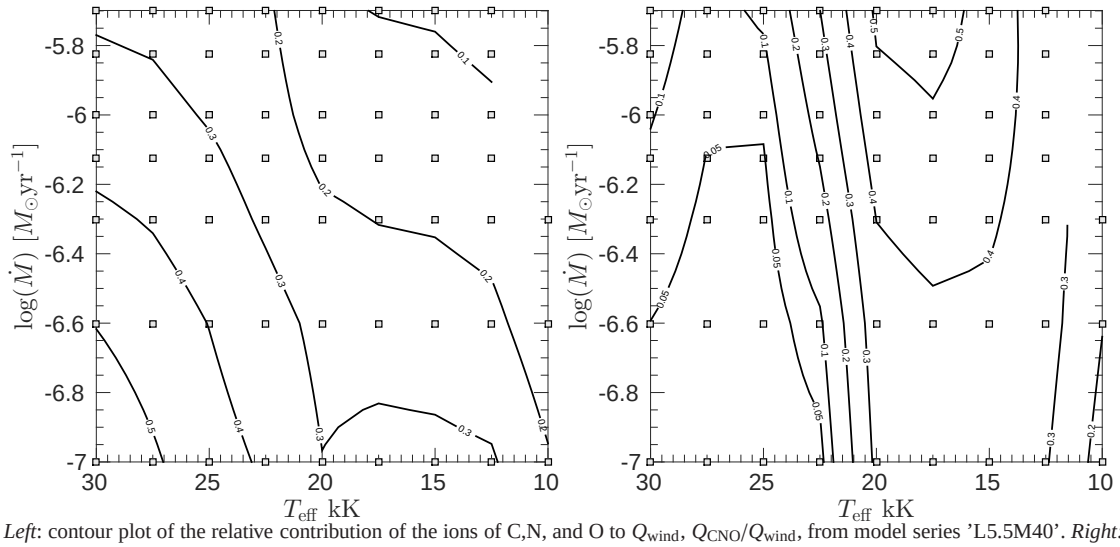

Figure 5. *Left*: contour plot of the relative contribution of the ions of C,N, and O to $Q_{\rm wind}$, $Q_{\rm CNO}/Q_{\rm wind}$, from model series 'L5.5M40'. *Right:* contour plot of the relative contribution of iron to $Q_{\rm wind}$, $Q_{\rm Fe}/Q_{\rm wind}$, for same models. For $T_{\rm eff} \geqslant 22\,500$ K $v_\infty/v_{\rm esc} = 2.6$, whilst for $T_{\rm eff} \leqslant 20\,000$ K $v_\infty/v_{\rm esc} = 1.3$.

is between ~10 000 and 8 800 K, which is the temperature range where Lamers et al. (1995) suspected that there might be a second bi-stability jump.

Figure 6 reveals that when $T_{\rm eff}$ is reduced below 10 000, Fe III recombines to Fe II, similarly to the recombination/ionisation of Fe IV/III already presented in Fig. 3. Note that at the coolest model, Fe III is not fully recombined to Fe II. Whereas in the inner (subsonic) part of the wind Fe II is the dominant ionisation stage, in the outer wind Fe III is still the dominant ion, even though Fe II contributes most to the total acceleration provided by iron, as shown in *right hand-side* of Fig. 2. If $T_{\rm eff}$ is further reduced, we anticipate Fe II to become the dominant ion throughout the wind and to provide an even larger fraction of the radiative acceleration.

The model with $T_{\rm eff} = 8\,800$ K from 'L5.5M40' series does not achieve $Q_{\rm wind} = 1$ at all when $\dot{M}$ is varied from 10^{-7} to 3×10^{-6} $M_\odot\,{\rm yr}^{-1}$. For such $T_{\rm eff}$, $Q_{\rm wind}$ becomes of order unity when metal abundances are increased (*cf.* § 3.4) or when models get close to the Eddington limit (Eddington 1921). The proximity to the Eddington limit is characterised by the *classical* Eddington factor:

$$\Gamma_e = \frac{\sigma_e L_\star}{4\pi c G M_\star} \qquad (6)$$

where σ_e is electron scattering opacity per unit mass and in the CGS system is measured in cm^2/g. In hot stars, σ_e is constant throughout the wind, as the majority of H and He ions are completely ionised. Thus, for early and mid Bsgs the Eddington factor depends only on the ratio between stellar luminosity and mass. However, for late Bsgs and Asgs this is no longer true.

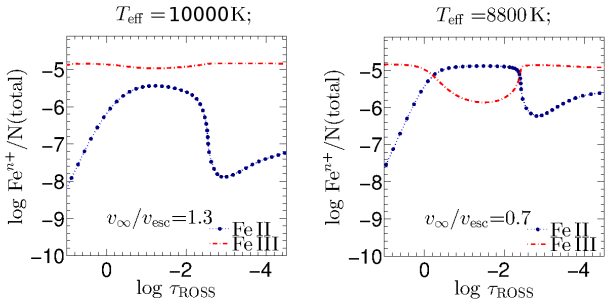

Figure 6. Change in ionisation balance between Feiii and Feii in models from 'L5.5M40' series with $\dot{M} = 0.25\times10^{-6}\,{\rm M}_\odot\,{\rm yr}^{-1}$.

We constructed our models close to the Eddington limit by decreasing the stellar mass, whilst the luminosity was kept fixed. We selected masses $M_\star$ = 20 and $M_\star$ = 30 $M_\odot$ for model series 'L5.5M20' and 'L5.5M30' respectively (*cf.* Table 2). The models with $T_{\rm eff}$ = 10 000 K obtain $Q_{\rm wind}$ = 1 at $\dot{M} \approx 0.09\times10^{-6}\,{\rm M}_\odot\,{\rm yr}^{-1}$ and $\dot{M} \approx 0.06\times10^{-6}\,{\rm M}_\odot\,{\rm yr}^{-1}$ for $M_\star$ = 20 and $M_\star$ = 30 $M_\odot$ respectively. However, the coolest model from 'L5.5M30' series still does not achieve $Q_{\rm wind}$ = 1 for $\dot{M}$ in range between 0.2 and $2\times10^{-6}\,{\rm M}_\odot\,{\rm yr}^{-1}$. The mass of the model has to be reduced to 20 $M_\odot$ in order for $Q_{\rm wind}$ to become unity. Thus, between 10 000 and 8 800 K CMFGEN predicts a jump in mass-loss rate, $\dot{M}_{\rm J}$, only in models series 'L5.5M20'.

According to Fig. 2 for the model with $T_{\rm eff}$ = 8 800 K Feii contributes mostly to the work ratio: it provides nearly 70% of $Q_{\rm wind}$. Thus, the predicted second jump in $\dot{M}$ should be caused by the radiative acceleration provided by Feii. This implies that mass-loss rates of late B/A supergiants and LBVs are sensitive to the ionisation equilibrium of iron. The reader should be aware that Feii is not fully recombined at $T_{\rm eff}$ = 8 800 K, and therefore we expect at cooler temperatures $\dot{M}_{\rm J}$ to increase further. This is very important for stellar evolution considerations.

3.4 The influence of metal abundances

The magnitude of $\dot{M}_{\rm J}$ depends on the metal composition. To investigate that, we have calculated a grid of models with solar metal abundances. Figure 7 compares contour plots of $Q_{\rm wind}$ in $\dot{M} - T_{\rm eff}$ plane for model series 'L5.5M40' with solar metal abundances. The observed velocity ratios are applied. It is interestingly to note that in model series 'L5.5M40' between 10 000 and 8 800 K, $\dot{M}$ at which $Q_{\rm wind}$ = 1 increases from ~ 0.06 to ~ $0.55\times10^{-6}\,{\rm M}_\odot\,{\rm yr}^{-1}$ (*cf.* Table 2), whilst for half-solar metallicities the coolest models did not acquired $Q_{\rm wind}$ = 1 at all. This implies that the second jump should be favoured in high metallicity environments, and for low metal environments, this jump is relevant only for objects close to the Eddington limit ($\Gamma \sim 1$).

If a constant velocity ratio of 1.3 is applied for the models with $T_{\rm eff}$ = 10 000 K and $T_{\rm eff}$ = 8 800 K and with half-solar metallicities, a second bi-stability jump is produced only when the models are close to the Eddington limit (*i.e.*'L5.5M20' model series). In 'L5.5M30' & 'L5.5M40' model series, a second BSJ is not produced at all when the constant velocity ratio of 1.3 is applied. This implies that the second BSJ in these series is a consequence of the applied observed velocity ratios.

To investigate in detail the origin of the second bi-stability jump, we show the total radiative acceleration in Fig. 8 in units of the local gravity (uppermost panels) as a function of λ and $\tau_{\rm ROSS}$

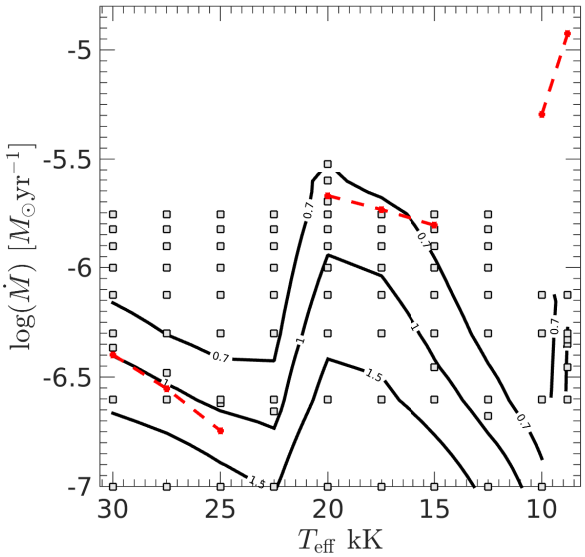

Figure 7. Contour plot of $Q_{\rm wind}$ in $\dot{M} - T_{\rm eff}$ plane for model series 'L5.5M40'. Models have solar metal composition and parameters as listed in Table 2. For comparison mass-loss rates calculated with the theoretical recipe of Vink et al. (2001) are shown with red dashed line.

for models with $T_{\rm eff}$ = 8 800 K (*left*) and $T_{\rm eff}$ = 20 000 K (*right*). For comparison, the radiative force due to the spectral lines of of Feii, Feiii, and CNO is displayed as well. In the cooler model, most of the radiative acceleration is provided by Feii, whilst in the hotter model Feiii is the dominant wind driver.

Note that there are white regions present in Fig. 8 where no information about radiative acceleration is revealed. Whilst in the second panel of the figure, the white regions are due to the lack of line transitions of the Feii ions with wavelengths (in Angstrom) $\log\lambda <\sim 2.95$ and $\log\lambda <\sim 3.1$, in the *left* uppermost panel, for $\log\lambda <\sim 2.9$, the white region is formed as a result of negative radiative flux, which may be related to a drop in the source function (*e.g.*, Owocki & Puls 1999). We tested the influence of the negative fluxes on the total radiative acceleration by setting their values to zero at the place where radiative force is computed. The total radiative acceleration did not change and therefore the impact of those fluxes on the radiative acceleration should be small.

In order to understand which frequencies are important, in Fig. 8 (fifth panel from the top) we also display the contribution of Feii (*left*) and Feiii (*right*) to $Q_{\rm wind}$ of the respective ions (blue lines). These contributions are normalised in such a way that the sum over all frequencies would equal unity. The red line (with ordinate in red colour placed on the *right-hand side*) shows the sum of the contributions of Feii (or Feiii in the right panel) located in different frequency bins. It is evident that about 50% of the acceleration of Feii comes from lines with λ between 2 300 and 2 800 Å, and the lines in the Balmer continuum provide more than 95% of total acceleration of Feii.

To understand the significance of these numbers, in the lowermost panels of the figure we present the contribution of Feii (left) and Feiii (right) to the *total* work ratio, provided by all ions. In the cooler model 40% of the total acceleration arises from lines with λ between 2 300 and 2 800 Å and the Feii lines in the Balmer continuum provide about 70% of the total acceleration. In the hotter

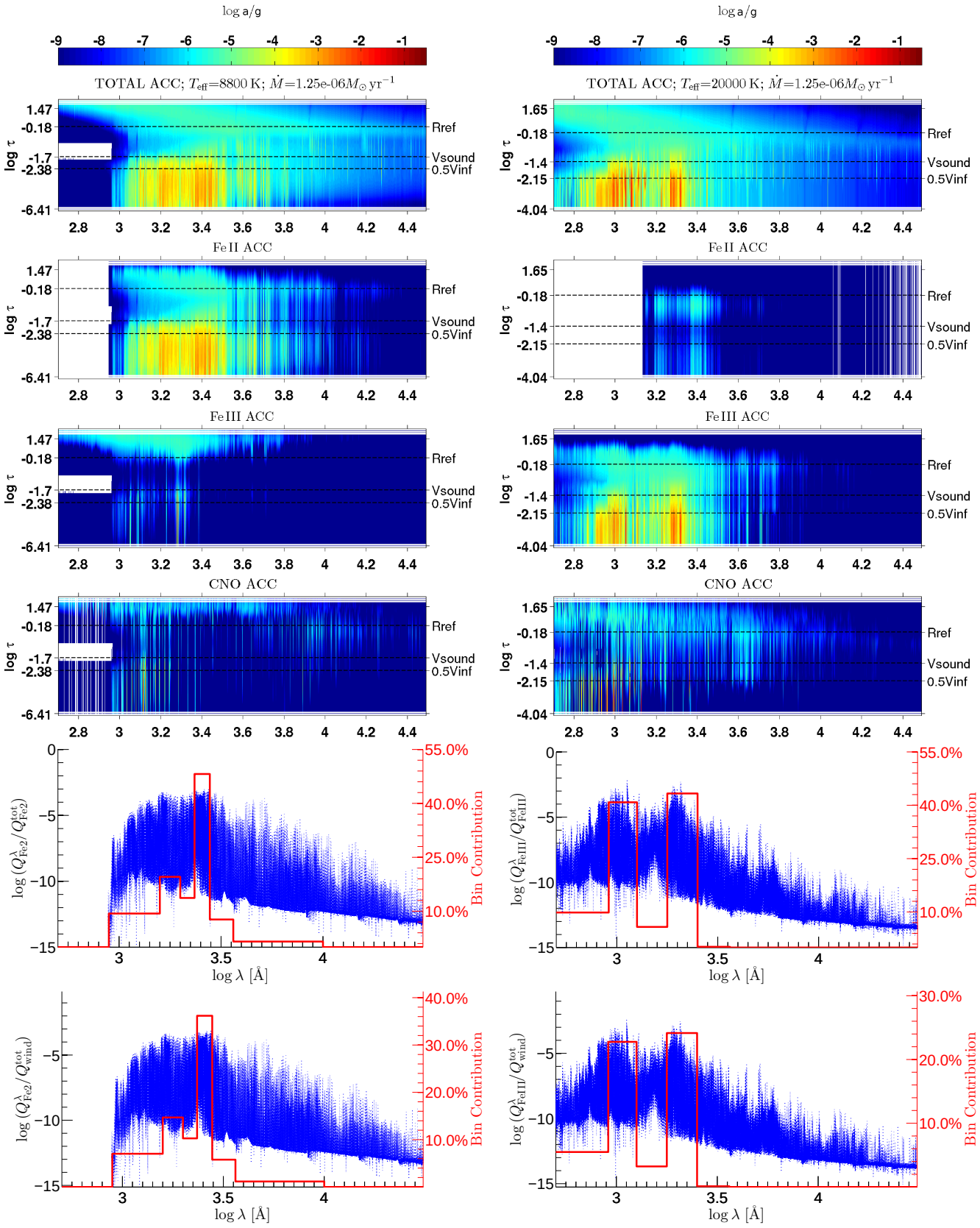

Figure 8. Radiative force provided by Fe II, Fe III, CNO, and all ions as a function of λ and $\tau_{\rm ROSS}$ for models with $T_{\rm eff}$ = 8 800 K (*left*) and $T_{\rm eff}$ = 20 000 K (*right*). Models have solar metal composition. The lowermost panels illustrate the contributions of the spectral lines to the work ratio obtained by the acceleration from Fe II (left) or Fe III (right). The red line (with ordinate on the *right-hand side*) presents the total contribution of spectral lines located in various frequency bins to the work ratio of Fe II (*left*) or Fe III (*right*).

Table 2. Mass-loss rates at which $Q_{\rm wind} = 1$ for different model series.

			$f_\infty = 0.1$; $v_{\rm cl} = 30\,{\rm km\,s^{-1}}$					$Z = Z_\odot$		$Z = Z_\odot/2$	
$\log \frac{L_\star}{L_\odot}$	$M_\star$	Γ_e	$\dot{M}$ range	$T_{\rm eff}$	$R_\star$	$\frac{v_\infty}{v_{\rm esc}}$	$\log g$	$\Gamma^*_{(\tau=2/3)}$	$\dot{M}_{Q_{\rm wind}=1}$	$\Gamma^*_{(\tau=2/3)}$	$\dot{M}_{Q_{\rm wind}=1}$
series name	$M_\odot$		$10^{-6}M_\odot$/yr	K	$R_\odot$				$10^{-6}M_\odot$/yr		$10^{-6}M_\odot$/yr
5.75	71	0.20	0.25 – 2.00	30 000	28	2.6	3.40	0.70	0.67	0.67	0.48
			0.25 – 2.00	27 500	33	2.6	3.25	0.67	0.51	0.63	0.39
L5.75M71			0.10 – 2.00	25 000	40	2.6	3.09	0.62	0.38	0.58	0.31
			0.10 – 2.00	22 500	49	2.6	2.90	0.58	0.30	0.55	0.24
			0.25 – 2.00	20 000	62	1.3	2.70	0.60	1.80	0.57	0.97
			0.25 – 2.00	17 500	81	1.3	2.47	0.61	1.55	0.57	0.75
			0.25 – 2.00	15 000	111	1.3	2.20	0.58	0.68	0.55	0.42
			0.10 – 2.00	12 500	159	1.3	1.88	0.57	0.28	0.55	0.22
			0.30 – 1.00	10 000	249	1.3	1.50	0.63	0.10	–	–
			0.48 – 1.50	8 800	–	0.7	1.27	0.75	0.48	–	–
5.50	40	0.20	0.10 – 2.00	30 000	21	2.6	3.40	0.71	0.39	0.67	0.28
			0.10 – 2.00	27 500	25	2.6	3.25	0.68	0.29	0.63	0.23
L5.5M40			0.10 – 2.00	25 000	30	2.6	3.09	0.62	0.22	0.58	0.18
			0.10 – 2.00	22 500	37	2.6	2.90	0.59	0.17	0.56	0.14
			0.10 – 2.00	20 000	46	1.3	2.70	0.61	1.14	0.57	0.58
			0.10 – 2.00	17 500	61	1.3	2.47	0.61	0.91	0.57	0.43
			0.10 – 2.00	15 000	83	1.3	2.20	0.57	0.38	0.55	0.24
			0.10 – 2.00	12 500	120	1.3	1.88	0.57	0.17	0.55	0.13
			0.04 – 1.00	10 000	187	1.3	1.50	0.63	0.06	0.62	0.05
			0.25 – 1.50	8 800	242	0.7	1.27	0.77	0.53	–	–
5.50	30	0.26	0.10 – 2.00	30 000	21	2.6	3.28	–	–	0.75	0.36
			0.10 – 2.00	27 500	25	2.6	3.13	–	–	0.73	0.28
L5.5M30			0.10 – 2.00	25 000	30	2.6	2.96	–	–	0.68	0.20
			0.10 – 2.00	22 500	37	2.6	2.78	–	–	0.64	0.16
			0.10 – 2.00	20 000	46	1.3	2.58	–	–	0.65	0.88
			0.10 – 2.00	17 500	61	1.3	2.34	–	–	0.67	0.60
			0.10 – 2.00	15 000	83	1.3	2.08	–	–	0.63	0.31
			0.10 – 2.00	12 500	120	1.3	1.76	–	–	0.63	0.16
			0.06 – 2.00	10 000	187	1.3	1.37	0.69	0.07	0.68	0.06
			0.20 – 2.00	8 800	242	0.7	1.27	0.79	1.43	–	–
5.50	20	0.39	0.07 – 0.50	10 000	187	1.3	1.19	0.79	0.12	0.78	0.09
L5.5M20			1.25 – 5.50	8 800	242	0.7	0.97	0.84	4.04	0.86	1.85

Notes. The *physical* Eddington factor, Γ, is distance dependent and therefore we show the value of Γ at the reference radius, where $\tau_{\rm ROSS} = 2/3$.

model, the Balmer continuum also provides a significant fraction of the total radiative force (about 50%).

According to Wien's displacement law, a black body with $T_{\rm eff} = 8\,800$ K peaks its radiative flux at $\lambda \sim 3\,300$ Å, which is near the wavelength interval where most of total line acceleration of the cooler model is provided. This is expected to support the total line force along with the larger fraction of Fe II. However, with a further decrease of $T_{\rm eff}$, despite the expected increase of the Fe II fraction, the overall radiation decreases, whilst furthermore the peak of radiation flux moves towards longer wavelengths. Thus, we do not expect that the size of the second bi-stability jump, if it were determined by models cooler than 8 800 K, to be significantly different from the one determined here between 10 000 and 8 800 K.

The theory of radiation-driven winds predicts that $\dot{M}$ depends on metallicity in the following way:

$$\dot{M} \propto Z^m \tag{7}$$

with

$$m = \frac{1-\alpha}{\alpha-\delta} \tag{8}$$

where α quantifies the ratio of the line force from optically thick lines to the line acceleration of all lines. The radiative acceleration is caused by an assortment of optically thin and thick lines and therefore α is between 0 and unity. The parameter δ was introduced by Abbott (1982) to account for variation of the ionisation throughout the wind (see also Kudritzki et al. 1989). The typical values for m are ranging from 0.5 (Kudritzki, Pauldrach, & Puls 1987) to 0.94 (Abbott 1982). Vink et al. (2001) found that $m = 0.69$ for O stars and $m = 0.64$ for B supergiants.

Figure 9 shows that the value of m strongly depends on $T_{\rm eff}$. $\dot{M}$ displays a weaker dependence on metallicity in the models with $T_{\rm eff} = 12\,500$ and 22 500 K, as Fe III is not an important line driver for these temperatures. Consequently, $\dot{M}$ becomes less sensitive to the adopted metal abundances. On the other hand, at $T_{\rm eff} = 20\,000$, Fe III is the dominant wind driver, and therefore the radiative acceleration becomes sensitive to metal abundance. Note that between 22 500 and 20 000 K m increases from 0.4 to 0.74, which indicates that the winds are driven by different ions.

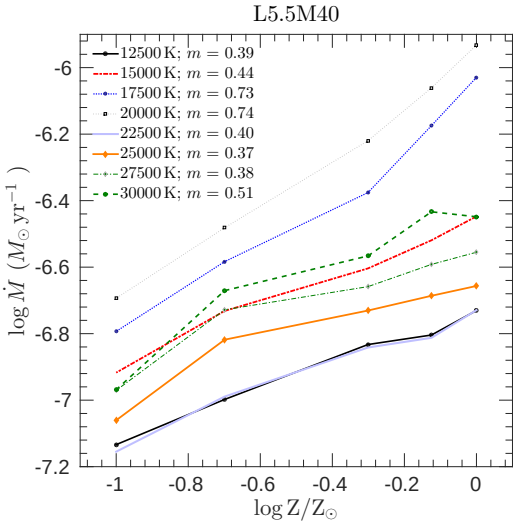

Figure 9. Stellar wind mass loss as a function of metallicity for models with different temperatures.

4 COMPARISON WITH MONTE-CARLO MASS-LOSS RATES

In Figure 7, we compare our results with the mass-loss rates following from the recipe of Vink et al. (2000, 2001), which are used both in observational work and in all up-to-date evolutionary models for massive stars. What complicates a meaningful comparison is the fact that the temperature location of the bi-stability jump predicted by CMFGEN and Monte-Carlo calculations is different. This means that we can only make rough comparisons between the two different methods, as it is not very meaningful to compare the mass-loss rate provided by one code at one $T_{\rm eff}$ to the mass-loss rate at the same $T_{\rm eff}$ by the other code. The differences we discuss in the following are thus only indicative. Due to the different temperature locations of the bi-stability jump in both methods, a prescribed $v_\infty/v_{\rm esc}$ value (corresponding to an option of '$v_\infty = -1$' in the script) in V00/V01 idl routine to calculate $\dot{M}$ is not appropriate to use (especially for models near BSJ). Instead, in the recipe we provide the absolute values of v_∞ in km s^{-1} as used in our CMFGEN models. We expect such a comparison to provide a better flavor of the differences between CMFGEN and V00/V01 mass-loss rates.

Because of the different temperature locations of the bi-stability jump in both codes, we compare our mass-loss rates to V00/V01 mass-loss rates for $T_{\rm eff} \geqslant 25\,000$ K, $T_{\rm eff}$ between 20 000 and 15 000 K, and for $T_{\rm eff} < 10\,000$ K , *i.e.* when in both methods the models are above, in between, or below the two bi-stability jumps. For L5.5M40 models series with solar metal abundance, we find the following (other cases lead to similar conclusions):

- above the first bi-stability jump ($T_{\rm eff} \geqslant 25\,000$ K), the mass-loss rates are similar
- CMFGEN predicts that the bi-stability jump should occur at lower temperature (between 22 500 and 20 000 K) in comparison to the theoretical expectations of V00/V01 (between 25 000 K and 22 500 K), which is in good agreement to the observations. Interestingly, the models just above the first BSJ according to V00/V01 have similar rates to those just above the first BSJ in CMFGEN, *i.e.* $\dot{M}^{25\,000}_{\rm vink} \approx \dot{M}^{22\,500}_{\rm Q_{xind}=1}$.
- over the first BSJ, in CMFGEN mass-loss rates are increased by a factor of 6 (4 for Z/Z$_\odot$ = 0.5), whilst over the second BSJ, mass-loss rates are increased by a factor of about 10. In CMFGEN, the size of both BS jumps is strongly dependent on the proximity of the models to the Eddington limit (*cf.* Fig. 10). On the other hand, according to V00/V01, both BS jumps should increase $\dot{M}$ roughly by a factor of ten, independent of metal abundances and the Eddington factor.
- despite that our models are inhomogeneous ($f_{\rm cl} = 0.1$), the recipe of V00/V01, which is based on homogeneous wind models, predicts higher $\dot{M}$ than CMFGEN[4]. Overall, the mass-loss rates in the cool Bsg range (between 20 000 and 15 000 K) are a factor of 2-5 lower than V00/V01 mass-loss rates. A possible reason for the lower mass-loss rates predicted by CMFGEN is that we are not sure whether we use all important driving lines, whilst Vink et al. (2000, 2001) pre-selected 10^5 relevant driving lines from millions bound-bound transitions for the first 30 elements in the Periodic Table. Furthermore, Vink et al. (2000, 2001) calculations are based on absolute solar metal abundances, $Z_\odot = 0.019$, taken from Anders & Grevesse (1989) which are larger than those determined by Asplund et al. (2009), used in this investigation.
- below the second BSJ, at $T_{\rm eff} = 8\,800$ K, V00/V01 rates are a factors of 6 to 40 larger than CMFGEN mass-loss rates. The largest discrepancy between Monte-Carlo predictions and CMFGEN is at $T_{\rm eff}$ =10 000 K, where V00/V01 mass-loss rates are a factor of 60 to 85 larger (*cf.* Fig. 7). Such a large discrepancy may be attributed to the different temperature locations of the second BSJ in CMFGEN and Monte-Carlo calculations. As an example, in the L5.5M40 model series the second BSJ is located between 10 000 and 8 800 K, whilst V00/V01 rates predict a second BSJ between 15 000 and 12 500 K. Consequently, at $T_{\rm eff} = 10\,000$ K, V00/V01 mass-loss rates are increased by the second BSJ, whilst in CMFGEN a second BSJ has not yet happened.

One should note that even in the absence of any bi-stability jumps (first or second) the overall mass-loss rate is expected to decrease with dropping $T_{\rm eff}$. Therefore, if one were to compare a hotter Monte-Carlo model with a cooler CMFGEN model, we would anticipate the Monte-Carlo model to have a higher $\dot{M}$ than the rate determined by the CMFGEN model, simply due to their different $T_{\rm eff}$. One should also be aware that most stellar evolution modellers 'switch' from Vink et al. (1999, 2000, 2001) to Nieuwenhuijzen & de Jager (1990) for cooler models. The relevance of this is that if we now find that the second jump takes place at lower $T_{\rm eff}$ than in the V00/V01 recipe, then the mass-loss rate in the stellar evolution models would be lower than assumed FOR THOSE TEMPERATURES. It remains to be investigated whether the overall mass lost would be affected significantly, as the dramatic increase may or may not fully take place at a lower $T_{\rm eff}$.

5 THE BI-STABILITY JUMP AND LUMINOUS BLUE VARIABLES

The bi-stability jumps, discussed in the previous section in the context of normal OB supergiants, might also play a role in the mass

[4] This is interesting because non-homogeneous models are expected to lead to higher mass-loss rates as the presence of clumping increases density inside the clumps which in turn increases the recombination rates. Consequently, the winds become less ionised. As lower ions have larger number of driving lines than the higher ones, the radiative force should increase (Muijres et al. 2011). Sundqvist et al. (2014) concluded that porosity in velocity space typically gives higher *empirical* mass-loss rates, but also a downward correction in theoretical mass-loss rates is possible if significant velocity-porosity at the wind critical point is present.

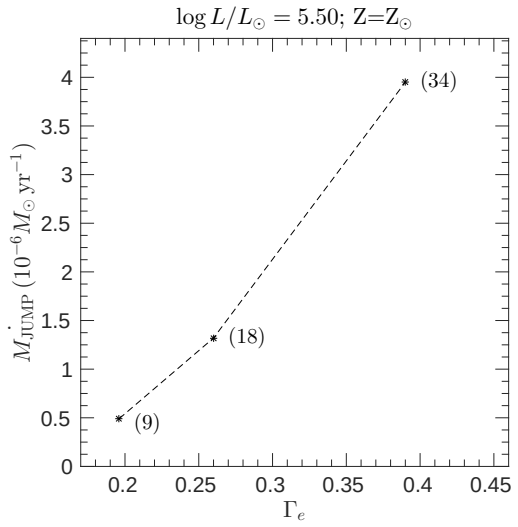

Figure 10. Dependence of the jump in $\dot{M}$ between 10 000 and 8 800 K on Eddington factor. The numbers in parentheses show the increase of mass loss rate across the second bi-stability jump in relative sense, *i.e.* $\dot{M}^{8\,800}_{Q_{\rm wind}=1}/\dot{M}^{10\,000}_{Q_{\rm wind}=1}$.

loss behaviour of LBVs. Based on the bi-stability mechanism, Vink & de Koter (2002) and Groh, Hillier, & Damineli (2011) were able to partly explain the behaviour of the $\dot{M}$ found by Stahl et al. (2001) during a typical LBV variation of AG CAR. However, in their calculations for LBV winds, the second jump occurred at a significantly hotter temperature ($T_{\rm eff} \simeq 20\,000$ K) in comparison to observations, whilst our CMFGEN calculations suggest that the second jump should occur at a cooler temperature ($T_{\rm eff} \simeq 10\,000$ K).

As the nature of LBVs is still under debate, their variable winds might offer key prospects to understanding their role as direct progenitors of SNe because both LBVs and SNe have shown double-troughed Hα line profiles, which can be explained if their wind changes instantaneously - as expected from the bi-stability jump (Trundle et al. 2008; Groh & Vink 2011).

Due to their high mass-loss rates LBVs have lost a considerable amount of mass during their evolution. Their luminosity-to-mass ratio is higher than for normal AB supergiants, and they might thus be in critical proximity to their Eddington limit (Humphreys & Davidson 1994; Vink 2012). It may thus be valuable to understand the influence of the Eddington factor on the size of the bi-stability jump.

In Fig. 10, the size of the jump between 10 000 and 8 800 K as a function of *classical* Eddington factor is illustrated. An increase of Γ_e leads to an increase in $\dot{M}_{\rm J}$, which is in agreement with the results of Vink & de Koter (2002) for LBVs and Vink (2006), Gräfener & Hamann (2008) and Vink et al. (2011) for very massive stars (VMS) as Of/WNh type objects. Across the second bi-stability jump mass-loss rates are increased by a factor of between 10 and 30. This is caused by two effects: i) an increase of $\dot{M}$ due to the second BSJ; and ii) an increase of $\dot{M}$ due to the Eddington limit. If such an increase of $\dot{M}_{\rm J}$ is real, we may expect to find different wind properties of objects located on both sides of this second jump, which would be particularly strong for objects close to the Eddington limit.

6 CONCLUSIONS

We have calculated a grid of wind models and predicted mass-loss rates of BA supergiants using the CMFGEN code. Our calculations independently confirm the bi-stability jump in $\dot{M}$ around $T_{\rm eff} \simeq 22\,500$ K predicted by Vink et al. (1999). However, CMFGEN predicts that this jump will occur at a lower temperature $T_{\rm eff} \simeq 20\,000$ K ($T_{\rm eff} = 17\,500$ K if clumping is not taken into account), which is consistent with observations.

In our models, the ions of C, N, and, O are the most important line "drivers" for $T_{\rm eff} > 22\,500$ K, whilst for temperatures between 20 000 and 12 500 K Fe III provides most of the radiative acceleration. For temperatures below 10 000 K, Fe III starts to recombine to Fe II and at $T_{\rm eff} = 8\,800$ K we find that Fe II provides most of the total line acceleration. This causes a second bi-stability jump in $\dot{M}$ around 8 800 K which is *dependent* on the Eddington parameter and metallicity. However, in many cases the V00/V01 recipe predicts a jump in $\dot{M}$ by a factor of about 10, *independent* of metal abundance or proximity to the Eddington limit. According to CMFGEN, this second jump also takes place at cooler temperature than the predicted temperature of the jump by V00/V01.

In the context of stellar evolution not only the discrepancies regarding the temperature position of the jump are important, but also the discrepancies in the absolute mass-loss rates. Most evolutionary models of massive stars use mass-loss rates from V00/V01 recipe. Consequently, the reported discrepancies between CMFGEN and Monte-Carlo predictions regarding the second bi-stability jump, imply that the mass-loss rates in late B and A-supergiants are likely too high, and need to be considered with caution when used in evolutionary calculations. Regarding the first jump the discrepancies between both methods are much smaller and the mass-loss rates are similar.

We found that at half-solar metal abundances a second BSJ is produced only in models close to the Eddington limit (with $\Gamma_e \sim 0.39$), whilst for normal BA supergiants the second BSJ is produced only for solar metal composition. Thus, for LBVs the second BSJ should be important even in low-metallicity environments and can be used as a tool to better understand the observed variations in their mass-loss rates. As the nature of LBVs is still not well understood, a detailed investigation of the second BSJ would be valuable.

A relevant question is whether the by CMFGEN predicted BS jumps in $\dot{M}$ are artificially produced due to the applied velocity ratios? We have demonstrated that for constant velocity ratio, CMFGEN predicts a jump in $\dot{M}$ between 22 500 and 20 000 K (Fig. 4), thus it is likely that the observed velocities are a consequence of an increase/drop in $\dot{M}$ around 21 000 K. However, this does not imply that the mass-loss rate varies with the same factor as the velocity ratios, because the reactions can be non-linear, due to the non-linear acceleration and the different elements which initiate and accelerate the wind. On the other hand, the second BSJ is only produced in models in close proximity to Eddington limit when the velocity ratio is kept fixed. This underlines the importance of both bi-stability jumps for LBVs. It is relevant to mention that the exact temperature of the bi-stability jumps remains somewhat ambiguous, as the ionisation equilibrium of Fe is sensitive to density and clumping properties in the lower wind and thus to stellar luminosity and mass.

Knowledge of the effects of clumping on the second bi-stability jump might be valuable, especially for LBVs, as they experience outbursts and episodes of enhanced mass loss during which the degree of clumping might change. Thus, the driving efficiency of Fe-group elements might be different for specific temperature

at various epochs during LBV phase. Therefore, it is important to quantify the effects of clumping on both sides of both bi-stability jumps (see Davies et al. 2007). Understanding all that, we might be able to explain some of the observed variations in $\dot{M}$ during the different phases of LBVs, with relevance for the properties of SN types IIb and IIn.

ACKNOWLEDGEMENTS

We acknowledge financial support from the Northern Ireland Department of Culture, Arts, and Leisure (DCAL) and the United Kingdom (UK) Science and Technologies Facilities Council (STFC). We gratefully thank Dr. John Hillier for providing the CMFGEN code to the astronomical community and Dr. Joachim Puls for his useful comments towards the improvement of the paper.

REFERENCES

Abbott D. C., 1982, ApJ, 259, 282
Abbott D. C., Lucy L. B., 1985, ApJ, 288, 679
Anders E., Grevesse N., 1989, Geochim. Cosmochim. Acta, 53, 197
Asplund M., Grevesse N., Sauval A. J., Scott P., 2009, ARA&A, 47, 481
Becker S. R., Butler K., 1995a, A&A, 294, 215
Becker S. R., Butler K., 1995b, A&A, 301, 187
Benaglia P., Vink J. S., Martí J., Maíz Apellániz J., Koribalski B., Crowther P. A., 2007, A&A, 467, 1265
Bestenlehner J. M. et al., 2014, A&A, 570, A38
Bouret J.-C., Lanz T., Hillier D. J., 2005, A&A, 438, 301
Crowther P. A., Lennon D. J., Walborn N. R., 2006, A&A, 446, 279
Davies B., Vink J. S., Oudmaijer R. D., 2007, A&A, 469, 1045
de Koter A., Schmutz W., Lamers H. J. G. L. M., 1993, A&A, 277, 561
Eddington A. S., 1921, Zeitschrift fur Physik, 7, 351
Ekström S. et al., 2012, A&A, 537, A146
Evans C. J. et al., 2011, A&A, 530, A108
Fullerton A. W., Massa D. L., Prinja R. K., 2006, ApJ, 637, 1025
Gal-Yam A. et al., 2014, Nature, 509, 471
Gal-Yam A., Leonard D. C., 2009, Nature, 458, 865
Garcia M., Herrero A., Najarro F., Lennon D. J., Urbaneja M. A., 2014, ArXiv e-prints
Gräfener G., Hamann W.-R., 2005, A&A, 432, 633
Gräfener G., Hamann W.-R., 2008, A&A, 482, 945
Gräfener G., Koesterke L., Hamann W.-R., 2002, A&A, 387, 244
Gräfener G., Vink J. S., 2016, MNRAS, 455, 112
Gräfener G., Vink J. S., de Koter A., Langer N., 2011, A&A, 535, A56
Groh J. H., 2014, A&A, 572, L11
Groh J. H., Hillier D. J., Damineli A., 2011, ApJ, 736, 46
Groh J. H., Meynet G., Ekström S., 2013, A&A, 550, L7
Groh J. H., Meynet G., Ekström S., Georgy C., 2014, A&A, 564, A30
Groh J. H., Vink J. S., 2011, A&A, 531, L10
Hillier J., Miller L., 1998, ApJ, 143, 62
Hummer D. G., Berrington K. A., Eissner W., Pradhan A. K., Saraph H. E., Tully J. A., 1993, A&A, 279, 298
Humphreys R. M., Davidson K., 1994, PASP, 106, 1025
Justham S., Podsiadlowski P., Vink J. S., 2014, ApJ, 796, 121
Khan R., Kochanek C. S., Stanek K. Z., Gerke J., 2015, ApJ, 799, 187
Kiewe M. et al., 2012, ApJ, 744, 10
Kotak R., Vink J. S., 2006, A&A, 460, L5
Kudritzki R. P., Pauldrach A., Puls J., 1987, A&A, 173, 293
Kudritzki R. P., Pauldrach A., Puls J., Abbott D. C., 1989, A&A, 219, 205
Kurucz R. L., 1988, in Astrophysics and Space Science Library, Vol. 138, IAU Colloq. 94: Physics of Formation of FE II Lines Outside LTE, Viotti R., Vittone A., Friedjung M., eds., p. 41
Lamers H. J. G. L. M., Snow T. P., Lindholm D. M., 1995, ApJ, 455, 269
Langer N., Hamann W.-R., Lennon M., Najarro F., Pauldrach A. W. A., Puls J., 1994, A&A, 290, 819
Maeder A., Meynet G., 2000, ARA&A, 38, 143
Markova N., Puls J., 2008, A&A, 478, 823
Martins F., Palacios A., 2013, A&A, 560, A16
Massa D., Fullerton A. W., Sonneborn G., Hutchings J. B., 2003, ApJ, 586, 996
McEvoy C. M. et al., 2015, A&A, 575, A70
Mokiem M. R. et al., 2007, A&A, 473, 603
Moriya T. J., Maeda K., Taddia F., Sollerman J., Blinnikov S. I., Sorokina E. I., 2014, MNRAS, 439, 2917
Muijres L. E., de Koter A., Vink J. S., Krtička J., Kubát J., Langer N., 2011, A&A, 526, A32
Muijres L. E., Vink J. S., de Koter A., Müller P. E., Langer N., 2012, A&A, 537, A37
Müller P. E., Vink J. S., 2008, A&A, 492, 493
Nahar S. N., 1995, A&A, 293, 967
Nieuwenhuijzen H., de Jager C., 1990, A&A, 231, 134
Nussbaumer H., Storey P. J., 1983, A&A, 126, 75
Nussbaumer H., Storey P. J., 1984, A&AS, 56, 293
Ofek E. O. et al., 2013, Nature, 494, 65
Oskinova L. M., Hamann W.-R., Feldmeier A., 2007, A&A, 476, 1331
Owocki S. P., 2015, in Astrophysics and Space Science Library, Vol. 412, Astrophysics and Space Science Library, Vink J. S., ed., p. 113
Owocki S. P., Gayley K. G., Shaviv N. J., 2004, ApJ, 616, 525
Owocki S. P., Puls J., 1999, ApJ, 510, 355
Pauldrach A. W. A., Puls J., 1990, A&A, 237, 409
Petrov B., Vink J. S., Gräfener G., 2014, A&A, 565, A62
Prinja R. K., Massa D. L., 2010, A&A, 521, L55
Puls J., Markova N., Scuderi S., Stanghellini C., Taranova O. G., Burnley A. W., Howarth I. D., 2006, A&A, 454, 625
Puls J., Springmann U., Lennon M., 2000, A&AS, 141, 23
Puls J., Vink J. S., Najarro F., 2008, A&A Rev., 16, 209
Repolust T., Puls J., Herrero A., 2004, A&A, 415, 349
Seaton M. J., 1987, Journal of Physics B Atomic Molecular Physics, 20, 6363
Shaviv N. J., 1998, ApJ, 494, L193
Shaviv N. J., 2000, ApJ, 532, L137
Shenar T. et al., 2015, ArXiv e-prints
Shiode J. H., Quataert E., 2014, ApJ, 780, 96
Smith N., 2015, in Astrophysics and Space Science Library, Vol. 412, Astrophysics and Space Science Library, Vink J. S., ed., p. 227
Smith N. et al., 2007, ApJ, 666, 1116
Stahl O., Jankovics I., Kovács J., Wolf B., Schmutz W., Kaufer A., Rivinius T., Szeifert T., 2001, A&A, 375, 54
Sundqvist J. O., Puls J., Feldmeier A., 2010, A&A, 510, A11

Sundqvist J. O., Puls J., Feldmeier A., Owocki S. P., 2011, A&A, 528, A64
Sundqvist J. O., Puls J., Owocki S. P., 2014, A&A, 568, A59
Trundle C., Kotak R., Vink J. S., Meikle W. P. S., 2008, A&A, 483, L47
Trundle C., Lennon D. J., 2005, A&A, 434, 677
Trundle C., Lennon D. J., Puls J., Dufton P. L., 2004, A&A, 417, 217
Šurlan B., Hamann W.-R., Kubát J., Oskinova L. M., Feldmeier A., 2012, A&A, 541, A37
van Genderen A. M., 2001, A&A, 366, 508
Vink J. S., 2006, in Astronomical Society of the Pacific Conference Series, Vol. 353, Stellar Evolution at Low Metallicity: Mass Loss, Explosions, Cosmology, Lamers H. J. G. L. M., Langer N., Nugis T., Annuk K., eds., p. 113
Vink J. S., 2012, in Astrophysics and Space Science Library, Vol. 384, Astrophysics and Space Science Library, Davidson K., Humphreys R. M., eds., p. 221
Vink J. S., 2015, in Astrophysics and Space Science Library, Vol. 412, Astrophysics and Space Science Library, Vink J. S., ed., p. 77
Vink J. S., Brott I., Gräfener G., Langer N., de Koter A., Lennon D. J., 2010, A&A, 512, L7
Vink J. S., de Koter A., 2002, A&A, 393, 543
Vink J. S., de Koter A., Lamers H. J. G. L. M., 1999, A&A, 350, 181
Vink J. S., de Koter A., Lamers H. J. G. L. M., 2000, A&A, 362, 295
Vink J. S., de Koter A., Lamers H. J. G. L. M., 2001, A&A, 369, 574
Vink J. S., Gräfener G., 2012, ApJ, 751, L34
Vink J. S., Muijres L. E., Anthonisse B., de Koter A., Gräfener G., Langer N., 2011, A&A, 531, A132
Zhang H., 1996, A&AS, 119, 523

APPENDIX A: MODEL ATOM (SOPHISTICATED MODELS)

Adopted atomic data of all elements included in our model atmosphere calculations are summarised in Table A1. The main source of atomic data comes from the Opacity project (Seaton 1987) and the Iron project Hummer et al. (1993). However, for some CNO elements, atomic data were used also from Nussbaumer & Storey (1983, 1984), whilst for Fe II, Fe III, Fe IV, and Fe VII data were used also from Nahar (1995); Zhang (1996); Becker & Butler (1995b,a) respectively.

In order to save computational time, at the different temperature regimes we choose, different (but relevant) level assignments for the involved ions.

Table A1. Atomic data included in our models

$T_{\rm eff}$ range [kK] Ion	8.8-10	12.5-20	22.5-27.5	30
H I	20/30	20/30	20/ 30	20/ 30
He I	45/69	45/69	45/ 69	45/ 69
He II	22/30	22/30	22/ 30	22/ 30
C I	22/42	–	–	–
C II	104/338	104/338	31/68	10,10,18
C III	91/209	91/209	99/243	99/243
C IV	–	19/24	59/64	59/64
C V	–	–	–	46/73
N I	22/35	–	–	–
N II	100/267	100/267	80/192	9/17
N III	–	41/82	41/82	41/82
N IV	–	13/23	78/124	200/278
N V	–	–	–	–
O I	32/161	13/29	–	–
O II	137/340	137/340	106/251	81/182
O III	–	165/343	165/343	165/343
O IV	–	9/16	99/202	71/138
O V	–	–	–	11/19
Ne II	42/242	42/242	42/242	25/116
Ne III	–	20/51	57/188	57/188
Mg II	22/65	18/36	–	–
Mg III	41/201	41/201	41/201	41/201
AL II	37/56	37/56	–	–
AL III	18/50	18/50	18/50	7/12
AL IV	–	46/107	46/107	62/199
Si II	27/53	27/53	–	–
Si III	81/147	81/147	81/147	26/51
Si IV	–	39/50	55/66	55/66
Si V	–	12/22	52/203	52/203
P IV	30/90	30/90	30/90	30/90
P V	–	9/15	9/15	9/15
S II	41/171	41/171	12/33	–
S III	80/257	80/257	80/257	41/83
S IV	–	49/138	69/194	69/194
S II		9/15	17/36	41/167
Ar III	29/249	29/249	29/249	18/82
Ar IV	–	8/22	29/97	41/204
Ca II	21/70	–	–	–
Ca III	41/208	41/208	41/208	41/208
Ca IV	–	2/3	33/171	39/341
Fe II	275/827	17/218	–	–
Fe III	136/1500	136/1500	136/1500	–
Fe IV	–	74/540	100/1000	100/1000
Fe V	–	17/67	34/352	45/869
Fe VI	–	–	–	55/674
Fe VII	–	–	–	13/50

Notes. For each ion, the number of super levels and full levels are provided.